Electronic Supplementary Material (ESI) for Journal of Materials Chemistry A.
This journal is © The Royal Society of Chemistry 2021

**SUPPORTING INFORMATION**

# Does the Seebeck Coefficient of Single Molecule Junctions Depend on the Junction Configuration?

František Vavrek,[Δa] Olena Butsyk,[Δa‡] Viliam Kolivoška,[a] Štěpánka Nováková Lachmanová,[a] Táňa Sebechlebská,[a$] Jakub Šebera,[a] Jindřich Gasior,[a] Gábor Mészáros[b] and Magdaléna Hromadová*[a]

[a] J. Heyrovský Institute of Physical Chemistry of the Czech Academy of Sciences, Dolejškova 3, 182 23 Prague 8, Czech Republic

[b] Research Centre for Natural Sciences, Eötvös Lóránd Research Network, Magyar Tudósok krt. 2, H-1117, Budapest, Hungary

## Table of Contents

## 1. Computational details

Molecules **1** and **2** were investigated for thermoelectric effect using density functional theory (DFT) method combined with non-equilibrium Green's function (NEGF) approach. Molecules were geometry optimized in vacuo without connection to gold electrodes using B3LYP functional[1] and 6-31G(d,p) basis set.[2–3] The geometry optimized molecules were inserted between two gold clusters $Au_{18}$ representing gold electrodes. The $Au_{18}$ cluster has the surface arrangement (111) and gold bond has the distance 2.885 Å corresponding to the Au bulk bond distance.[4] The geometry of $Au_{18}$ clusters was fixed during geometry optimization of the molecular junction (MJ) system $Au_{18}$–molecule–$Au_{18}$. The geometry optimization of the molecular junction was performed by B3LYP method including dispersion coefficient D3[5] with 6-31(d) basis set[2–4] for N, C, H atoms and LANL2DZ basis set[6] for Au atoms. In order to find the potential energy minimum of the system and the optimal distance between two gold electrodes we varied the distance ($z$) between centers of the apex atoms of the gold clusters in the steps of 0.1 Å. This distance varied from 11.3 Å to 11.9 Å for MJ of molecule **1** and from 14.5 Å to 16.7 Å for MJ of molecule **2**, respectively. All geometry optimization tasks were performed by Gaussian 09 program.[7] The theoretical MJ length $z^{th}$ represents the MJ length corrected for the distance between centers of two gold atoms in contact, i.e. $z^{th} = z - 2.5$ Å. Three types of theoretical MJ length values were identified: full MJ optimized value $z_{opt}^{th}$, optimized MJ value with fixed electrode distance corresponding to experimentally obtained MJ length for high conductance ($z_H^{th} = z_H^{exp}$) and low conductance ($z_L^{th} = z_L^{exp}$) MJ length. We used the knowledge of $z^{exp}$ and created the MJ model where the distance of centers of apex atoms of the gold clusters is the value based on $z^{exp}$ (model is the same as geometry optimized except that the distance between centers of two gold atoms in contact is fixed) or the model where two parallel surfaces of gold clusters are against each other and $z^{exp}$ indicates the distance between surfaces of individual gold clusters (this surface goes through centers of atoms on the surface of gold clusters). The gradient-optimized energy minima structures were used for transmission function $\tau(E)$ calculations by NEGF approach. DFT calculations of the transmission functions were provided by PBE0 functional including 25 % HF exchange contribution.[8] The method where self-energy of the semi-infinite electrodes is calculated was used. Recently in our group, the PBE0 DFT functional was successfully used for interpretation of STM-BJ experiment.[9,10]

For the transmission function calculations, the double-$\zeta$ plus polarization function (DZP) basis sets were used for N, C, H atoms and Au atoms were described by DZ basis set.[11] For our calculations the frozen-core Slater-type basis sets were used. The reliability of the calculations with the frozen-core approximation in connection with the hybrid DFT functionals is discussed in Ravelli *et al.*[12] For DFT calculations of transmission functions the scalar-relativistic zero-order regular approximation SR-ZORA approach[13,14] as implemented in ADF 2017 program[15] was used. The conductance (in the zero–bias approximation) was calculated based on Landauer equation $G = G_0 \times \tau(E_F)$, where $G_0$ is the conductance quantum and $\tau(E_F)$ is the transmission function at the Fermi level $E_F$ of the gold electrodes.[16,17] We used Fermi level $E_F = -5.1 \pm 0.1$ eV against vacuum obtained from the experimental work function of polycrystalline gold.[18]

The conductance was calculated from the transmission function in the energy interval from –5.0 to –5.2 eV and the average of individual points in this interval was used for determination of $G$. Thermopower (Seebeck coefficient) was calculated based on the Equation (2) of the main text, for which the natural logarithm of the transmission function was numerically differentiated in the energy interval from –5.0 to –5.2 eV and the average of these values was used for the calculation of Seebeck coefficient using T = 300 K.

## 2. STM-BJ design incorporating an open circuit OFF state configuration

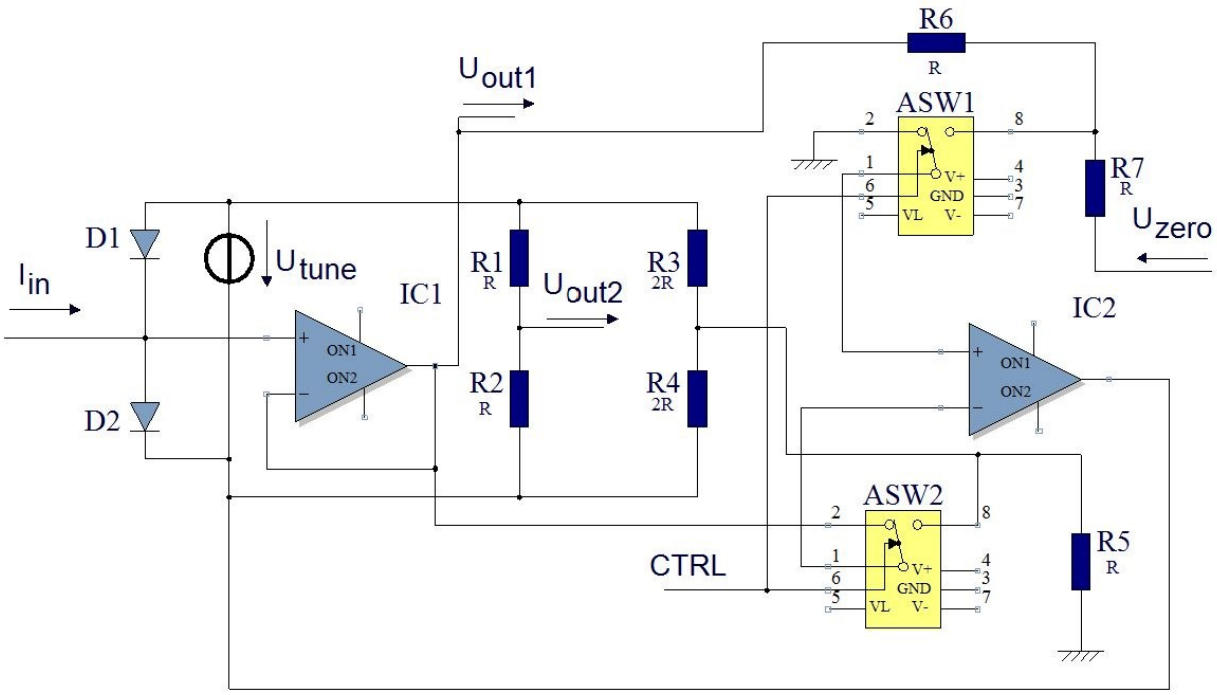


**Figure S1** Simplified scheme of the tunable bipolar logarithmic *I–V* converter with realization of ON ($V_{bias}$ applied, current measured) and OFF (open circuit, residual voltage $V_{res}$ measured) states. Changing $U_{tune}$ permits the improvement of speed at the expense of current resolution and *vice versa*. The ON/OFF state is determined by the logic level CTRL signal (ON: CTRL = LOW, OFF: CTRL = HIGH). The settings of the analog switches correspond to the ON state in the presented scheme.

### *Initialization of the measuring procedure*

Procedures leading to minimization of the residual current need to be performed prior to the simultaneous *G* and *S* measurements. The tip is connected to the input of the *I–V* converter which keeps it at virtual ground in the ON state while measuring the current flowing through the tip using $U_{out2}$ as output signal. At the same time, the substrate electrode is kept at $-V_{bias}$ level. In the OFF state (CTRL = HIGH) the *I–V* converter acts as a current generator issuing zero current. The potential of the tip is reflected in $U_{out1}$ output. During the OFF state the potential of the substrate is switched to signal ground level. For the best measurement of the residual thermal voltage in the OFF period there is a possibility to adjust the potential of the substrate to compensate the input offset voltage of the IC1 operational amplifier. $U_{zero}$ serves for the minimization of the input leakage current in the OFF state. For that calibration, first the input of the switched off *I–V* converter is directly connected to ground, then secondly through a very high value (10 GΩ) resistor. In the calibrated state $U_{out1}$ should show the same level in both cases.

### *Fast Fourier transform (FFT) spectra calculation and data filtering*

The FFT spectra calculation and filtering procedures were applied on residual voltage $V_{res}$ data recorded during conductance trace measurements of molecule **2** obtained in $G_L$ regime of Au–molecule–Au junction. Figure S2 shows $V_{res}$ histograms of the original data (a) and filtered data (b). Processed data were obtained at all noted values of temperature difference $\Delta T$ applied between the electrodes during measurements. Both tasks of calculating FFT spectra and filtering

were performed by OriginPro scientific graphing and data analysis software (OriginPro, Version 9.1 OriginLab Corporation, Northampton, MA, USA). Residual voltage data were recorded at 16.667 kHz sampling rate, permitting an 8 kHz bandwidth of the spectra. The length of the individual trace data samples varied from ~1500 to ~12000 datapoints only, resulting in frequency resolution of individual spectra ranging from ~1.4 to ~10.7 Hz. Since the discontinuity of data sampled in time domain due to omission of datapoints recorded in ON state (see main text for details), these needed to be preprocessed by connecting the adjacent data segments into a single string of continuous time-domain data. Preprocessed data of selected samples with length of ~3000 datapoints are shown as black lines on the left-hand side graphs in Figure S3.

FFT spectrum was calculated for each individual trace data sample separately. Samples were processed as whole, with no subdivisions into smaller sets and window overlapping. Due to requirements of high resolution and sensitivity, rectangular window was applied. Calculated FFT spectra in terms of amplitude vs. frequency for selected trace samples are shown as black lines on the right-hand side graphs in Figure S3. The AC power-line noise depicted as the highest peak at its fundamental frequency of 50 Hz is present in all spectra, confirming its strong contribution to the recorded signal. The occurrence of second major noise contribution in the form of harmonic series with fundamental frequency of 300 Hz is notable as well. The data obtained at the lowest temperature difference of $\Delta T$ = –8.0 K (top right panel with black and violet lines in Figure S3) contain in addition to fundamental frequency of 50 Hz signal at multiples of 600 Hz and 1450 Hz frequencies. Based on results from calculated FFT spectra, individual data samples were subsequently filtered with a series of software-based rectangular band-stop filters. Bandwidths of the filters were set for each individual data sample separately based on the position and the broadening of noise peaks near the frequency values of characteristic noise peaks (50 Hz, 300 Hz, 600 Hz, etc.). Figure S3 shows the original (black line) and filtered (colored lines) $V_{res}$ data of selected samples as well as their FFT spectra calculated before (black) and after (colored) the application of filters.

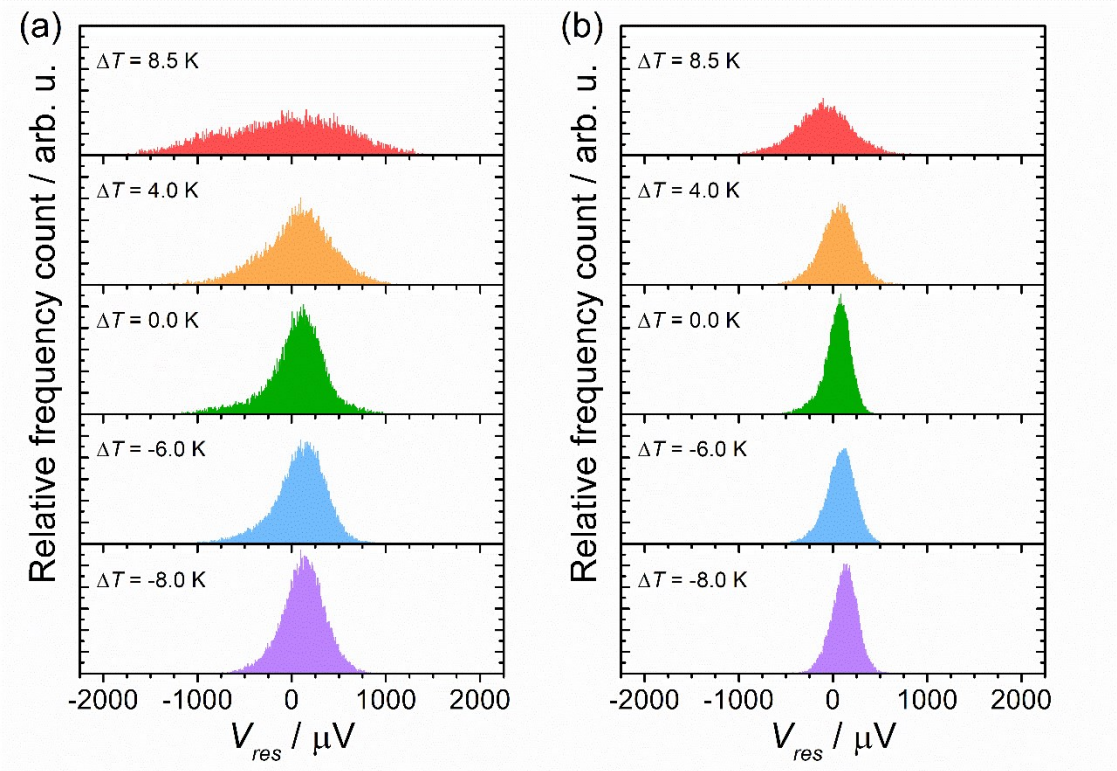


**Figure S2** Normalized histograms of residual voltage $V_{res}$ for MJs of molecule **2** obtained in low conductance regime before (a) and after (b) filtering procedure. Temperature difference between substrate and tip electrodes was $\Delta T$ = 8.5 K (red), $\Delta T$ = 4.0 K (orange), $\Delta T$ = 0 K (green), $\Delta T$ = –6.0 K (blue) and $\Delta T$ = –8.0 K (violet), respectively.

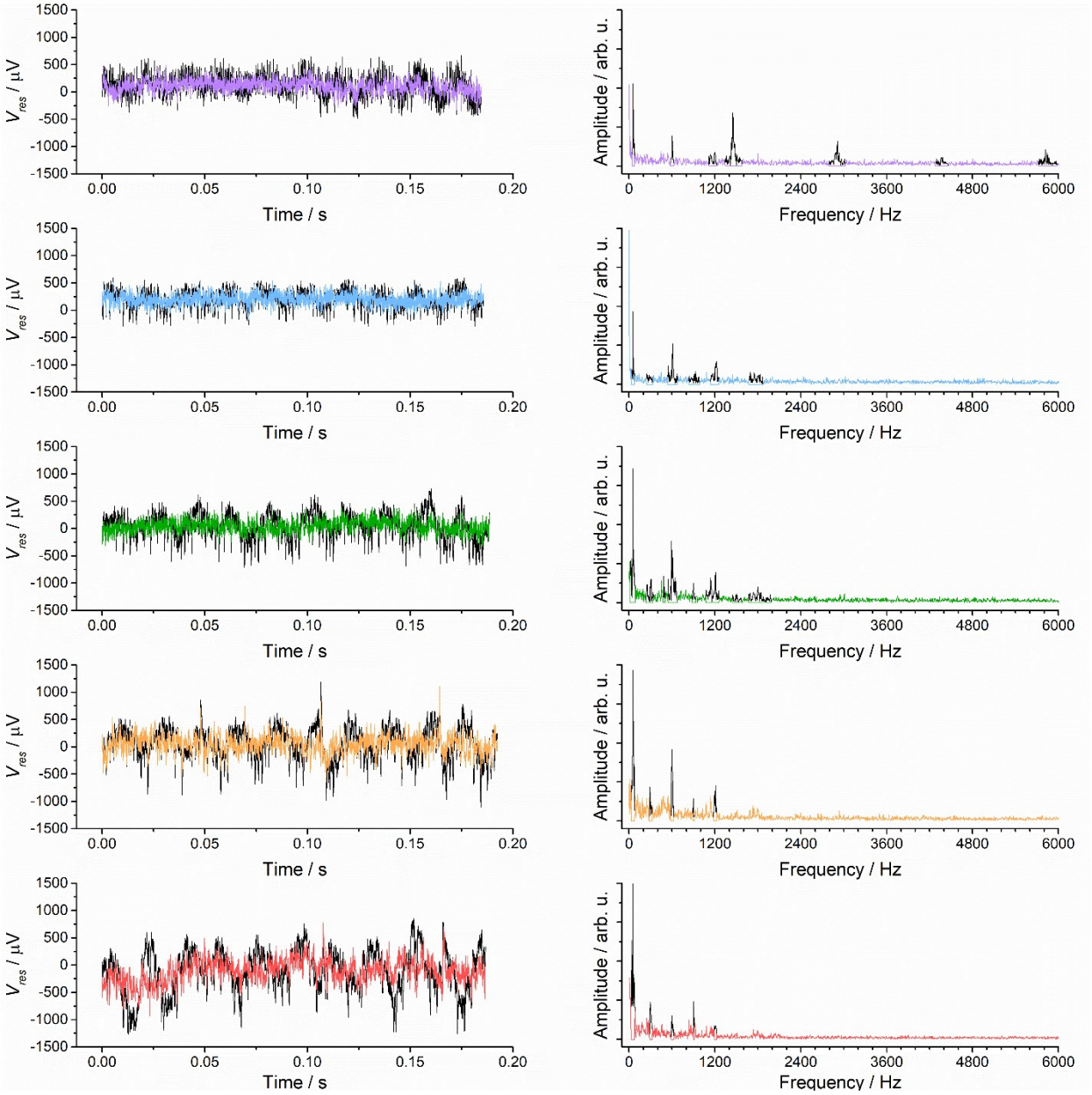


**Figure S3** Selected individual trace data samples of residual voltage $V_{res}$ recorded during conductance trace measurements of molecule **2** in $G_L$ regime of Au–molecule–Au junction formation (left) and corresponding calculated FFT spectra (right). Black lines represent the voltage $V_{res}$ data and FFT spectra of the preprocessed original data samples. Colored lines are voltage data and FFT spectra of data samples after filtration procedure. Different values of temperature difference $\Delta T$ applied between the electrodes equal to –8.0 K (violet), –6.0 K (blue), 0 K (green), 4.0 K (orange) and 8.5 K (red), respectively.

### 3. Quantum chemical calculations of *G* and *S* values

Values $S(G_{opt})^{th}$ refer to a model with fully extended and optimized single molecule junction configuration for **1** and **2** (see Table S1, Figs. S4 and S5) representing the low conductance regime. This model reproduced correctly the sign of Seebeck coefficient for both molecules, but did not provide reasonable agreement with $S(G_L)^{exp}$ for molecule **1**.

Subsequently, modified models of MJ configurations (see Table S2, Figs. S6 and S7) used fixed characteristic distance between gold electrodes to define the junction in a desired (high or low) conductance regime. Theoretical MJ length values $z^{th}$ used in these computational models were within the experimentally observed range of MJ length values. Table 1 of the main text compares calculated theoretical $S(G_H)^{th}$ and $S(G_L)^{th}$ values with their experimental counterparts. New computational model for MJs of molecule **1** (see Fig. S6) improved the agreement between experimental and theoretical *G* and *S* values. $S(G_H)^{th}$ for **1** practically coincides with the observed $S(G_H)^{exp}$ value and is slightly less negative than $S(G_L)^{exp}$. Even better agreement was observed for molecule **2** between theory and experiment. For theoretical MJ configurations see Fig. S7. Both calculated $S(G_H)^{th}$ and $S(G_L)^{th}$ values are similar in magnitude and only slightly underestimated the experimental thermopower values.

Finally, we have considered the possibility of a van der Waals dimer formation within the molecular junction of **1** and **2** to complete our theoretical studies. Magyarkuti *et al.*[19] suggested this possibility for the $G_L$ state of molecule **2** and stated that molecule **1** does not form this type of junctions. Our theoretical results are summarized in Table S3 and Fig. S8. In agreement with Magyarkuti *et al.*[20] we have observed that the dimer MJ configuration for molecule **1** does not lead to thermopower values experimentally observed, whereas that for molecule **2** gave theoretical MJ conductance and thermopower values comparable with the experimental ones in the low conductance regime (compare Table 1 and Table S3). The $\log(G_L/G_0)^{exp}$ for **2** is better reproduced by this dimer model compared to the single molecule MJ configuration, whereas $S(G_L)^{th}$ is +13.2 μV $K^{-1}$ for the dimer MJ and +8.5 μV $K^{-1}$ for the single molecule MJ model. Since $S(G_L)^{exp}$ = +10.4 ± 3.0 μV $K^{-1}$, it is quite difficult to decide which model describes better our experimental results. In both cases (if we consider two instead of one molecule within the junction) the Seebeck coefficient falls within the experimentally obtained data range. This observation gives further support to the statement of Reddy *et al.*[20] who postulated that thermopower of MJ is independent of the number of molecules, since it is the intensive property of the matter.

## *Optimized (minima on potential energy curve along z) single molecule junction configurations*

**Table S1** DFT computed characteristic parameters (conductance, junction length, torsion angle between two aromatic rings and Seebeck coefficient) for geometrically fully optimized MJ of molecules **1** and **2**.

| MJ | $\log(G_{opt}/G_0)^{th}$ | $z_{opt}{}^{th}$/ nm | $\theta$ / ° | $S(G_{opt})^{th}$/ μV K$^{-1}$ |
|---|---|---|---|---|
| **1** | –3.28 | 0.9 | 37.3[a] | –22.8 |
| **2** | –3.19 | 1.3 | 0.0 | 8.7 |

[a] angle $\theta$ between the planes of two aromatic rings (see Figure S4 below)

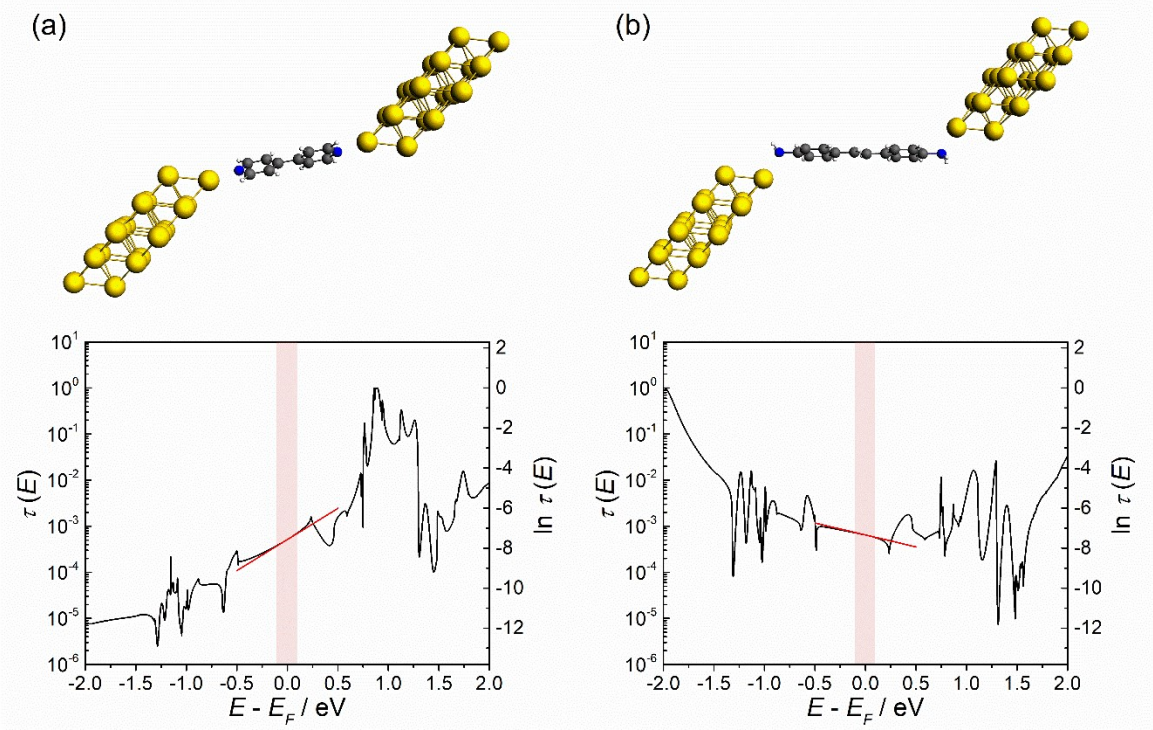


**Figure S4** Geometry optimized MJ configuration (top) and MJ transmission function $\tau(E)$ (bottom) for molecule **1** (a) and molecule **2** (b). The MJ length corresponded to the geometry of the system with minimized potential energy. Red line represents the derivative $\partial \ln\tau(E)/\partial E$ at $E = E_F$.

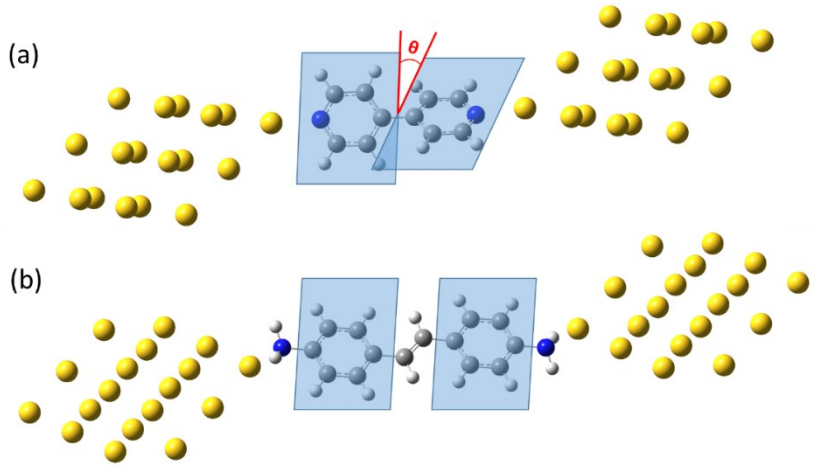


**Figure S5** Schematic presentation of the definition of angle $\theta$ between two planes of the aromatic rings for MJ of molecule **1** (a) and **2** (b).

## *Single molecule junction configuration with MJ length fixed to experimentally observed value*

**Table S2** DFT-computed characteristic parameters (conductance, MJ length, and Seebeck coefficient) for two (high and low) MJ configurations.

| MJ | $\log(G_H/G_0)^{th}$ | $z_H^{th}$/ nm | $\log(G_L/G_0)^{th}$ | $z_L^{th}$/ nm | $S(G_H)^{th}$/ μV K$^{-1}$ | $S(G_L)^{th}$/ μV K$^{-1}$ |
|---|---|---|---|---|---|---|
| **1**[a] | –3.13 | 0.7 | –4.33 | 0.9 | –7.0 | –3.6 |
| **2**[b] | –3.17 | 1.0 | –3.20 | 1.3 | +9.4 | +8.5 |

[a] fixed plane distance, [b] fixed apex atom distance

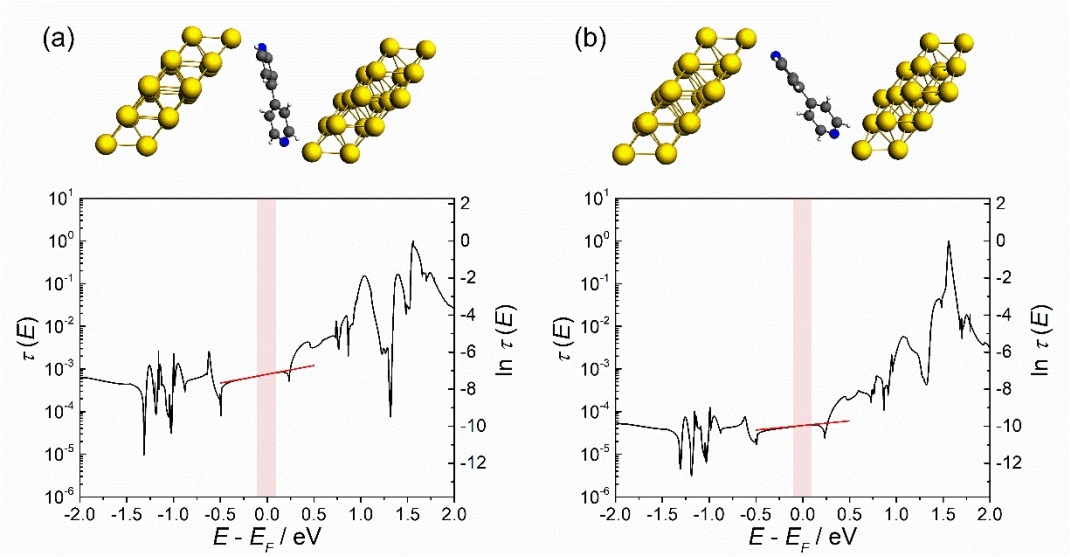


**Figure S6** Geometry optimized MJ configuration (top) and MJ transmission function $\tau(E)$ (bottom) for molecule **1** at two different MJ length values corresponding to high (a) and low (b) conductance system. Experimental MJ length values were simulated by a constant distance between two parallel gold electrode planes. Red line represents the derivative $\partial \ln\tau(E)/\partial E$ at $E = E_F$.

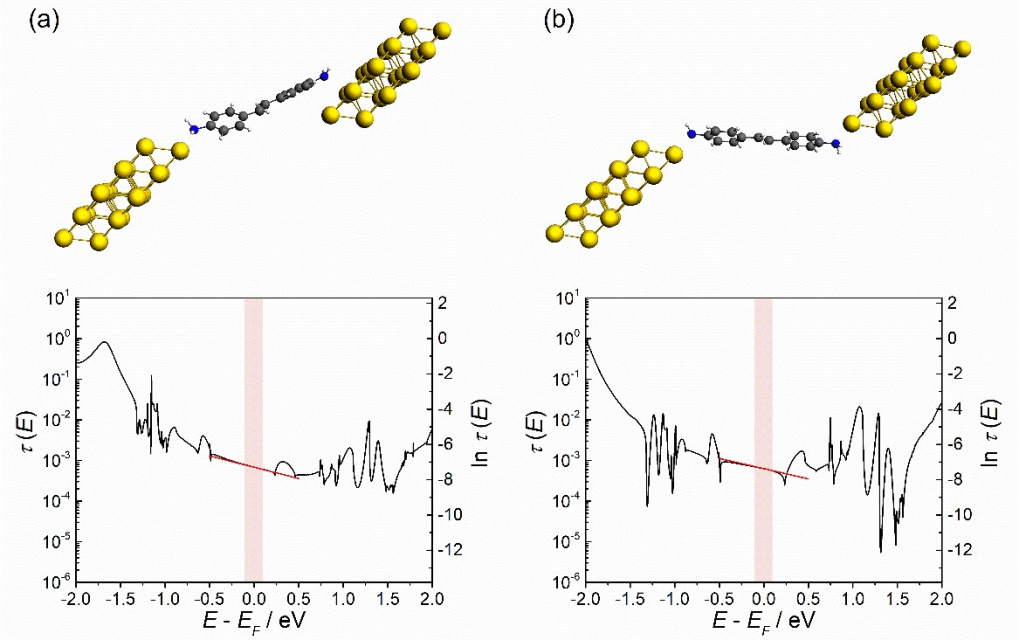


**Figure S7** Geometry optimized MJ configuration (top) and MJ transmission function $\tau(E)$ (bottom) for molecule **2** at two different MJ length values corresponding to high (a) and low (b) conductance system. Experimental MJ length values were simulated by a constant distance between two apex gold atoms of the electrode. Red line represents the derivative $\partial \ln\tau(E)/\partial E$ at $E = E_F$.

**Table S3** DFT-computed single molecule conductance, MJ length and Seebeck coefficient for low conductance MJ configuration containing face-to-face dimer.

| MJ | $\log(G_L/G_0)^{th}$ | $z_L^{th}$/ nm | $S(G_L)^{th}$/ μV K$^{-1}$ |
|---|---|---|---|
| **1**–**1**[a] | –5.96 | 1.2 | –23.6 |
| **2**–**2**[a] | –4.03 | 1.5 | +13.2 |

[a] fixed apex atom distance

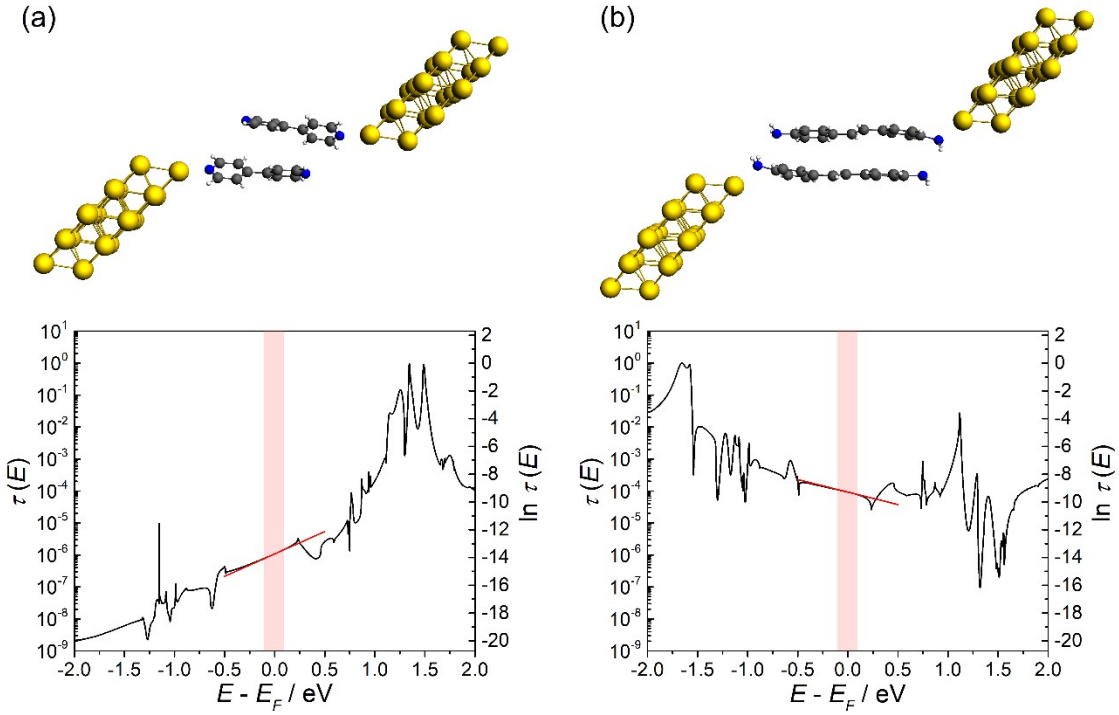


**Figure S8** Geometry optimized MJ configuration (top) and MJ transmission function $\tau(E)$ (bottom) for junction containing two molecules of **1** (a) or **2** (b). The MJ length values for this low conductance system $z_L^{th}$ were fixed to a constant distance between two apex gold atoms of the electrodes. Red line represents the derivative $\partial \ln\tau(E)/\partial E$ at $E = E_F$.

## References


[1] A. D. Becke, *J. Chem. Phys.*, 1993, **98**, 5648–5652.
[2] R. Ditchfield, W. J. Hehre and J. A. Pople, *J. Chem. Phys.*, 1971, **54**, 724–728.
[3] W. J. Hehre, R. Ditchfield and J. A. Pople, *J. Chem. Phys.*, 1972, **56**, 2257–2261.
[4] M. M. Mariscal, O. A. Oviedo and E. P. M. Leiva, *Metal clusters and nanoalloys: from modeling to applications*. Springer Science & Business Media, 2012.
[5] S. Grimme, J. Antony, S. Ehrlich and H. Krieg, H. *J. Chem. Phys.*, 2010, **132**, 154104 (19 pp).
[6] P. J. Hay and W. R. Wadt, *J. Chem. Phys.*, 1985, **82**, 299–310.
[7] M. J. Frisch, G. W. Trucks, H. B. Schlegel, G. E. Scuseria, M. A. Robb, J. R. Cheeseman, G. Scalmani, V. Barone, G. A. Petersson, H. Nakatsuji, X. Li, M. Caricato, A. V. Marenich, J. Bloino, B. G. Janesko, R. Gomperts, B. Mennucci, H. P. Hratchian, J. V. Ortiz and A. F. Izmaylov *et al. Gaussian 09 Rev. E.01*, Wallingford, CT, 2013.
[8] C. Adamo and V. Barone, *J. Chem. Phys.*, 1999, **110**, 6158–6169.
[9] J. Šebera, V. Kolivoška, M. Valášek, J. Gasior, R. Sokolová, G. Mészáros, W. Hong, M. Mayor and M. Hromadová, *J. Phys. Chem. C*, 2017, **121**, 12885–12894.
[10] J. Šebera, M. Lindner, J. Gasior, G. Mészáros, O. Fuhr, M. Mayor, M. Valášek, V. Kolivoška and M.

Hromadová, M. *Nanoscale*, 2019, **11**, 12959–12964.
[11] E. van Lenthe and E. J. Baerends, *J. Comput. Chem.*, 2003, **24**, 1142–1156.
[12] D. Ravelli, D. Dondi, M. Fagnoni, A. Albini and A. Bagno, *J. Comput. Chem.*, 2011, **32**, 2983–2987.
[13] E. van Lenthe, A. Ehlers and E. J. Baerends, *J. Chem. Phys.*, 1999, **110**, 8943–8953.
[14] E. van Lenthe, E. J. Baerends and J. G. Snijders, *J. Chem. Phys.*, 1993, **99**, 4597–4610.
[15] G. te Velde, F. M. Bickelhaupt, E. J. Baerends, C. Fonseca Guerra, S. J. van Gisbergen, J. G. Snijders and T. Ziegler, *J. Comput. Chem.*, 2001, **22**, 931–967.
[16] S. Datta *Electronic transport in mesoscopic systems*. Cambridge university press, 1997.
[17] R. Landauer *J. Phys. Condens. Matter*, 1989, **1**, 8099–8110.
[18] S. Veenstra, U. Stalmach, V. Krasnikov, G. Hadziioannou, H. Jonkman, A. Heeres and G. A. Sawatzky, *Appl. Phys. Lett.*, 2000, **76**, 2253–2255.
[19] A. Magyarkuti, O. Adak, A. Halbritter and L. Venkataraman, *Nanoscale*, 2018, **7**, 3362–3368.
[20] P. Reddy, S.-Y. Jang, R. A. Segalman and A. Majumdar, *Science*, 2007, **315**, 1568–1571.